

JWST observations of segregated $^{12}\text{CO}_2$ and $^{13}\text{CO}_2$ ices in protostellar envelopes

N. G. C. Brunken,^{*,†} A. C. A. Boogert,[‡] E. F. van Dishoeck,^{¶,†} N. J. Evans,[§] C. A. Poteet,^{||} K. Slavicinska,[†] L. Tychoniec,[†] P. Nazari,[⊥] L. W. Looney,[#] H. Tyagi,[@] M. Narang,[@] P. Klaassen,[△] Y. Yang,[▽] P. J. Kavanagh,^{††} S. T. Megeath,^{‡‡} and M. E. Ressler^{¶¶}

[†]*Leiden Observatory, 2300 RA Leiden, The Netherlands*

[‡]*Institute for Astronomy, University of Hawai'i at Manoa 2680 Woodlawn Drive, Honolulu, HI 96822, USA*

[¶]*Max-Planck-Institut für Extraterrestrische Physik, Gießenbachstraße 1, 85748 Garching, Germany*

[§]*Department of Astronomy, The University of Texas at Austin, 2515 Speedway, Stop C1400, Austin, Texas 78712-1205, USA*

^{||}*NV5 Geospatial Solutions, Inc. 385 Interlocken Crescent, Suite 300 Broomfield, CO 80021, USA*

[⊥]*European Southern Observatory, Karl-Schwarzschild-Strasse 2, 85748 Garching bei München, Germany 510*

[#]*Department of Astronomy, University of Illinois, 1002 W. Green St., Urbana, IL, 61801*

[@]*Department of Astronomy and Astrophysics Tata Institute of Fundamental Research 4 Homi Bhabha Road, Colaba, Mumbai 400005, India*

[△]*United Kingdom Astronomy Technology Centre, Edinburgh, Blackford Hill, Edinburgh, EH9 3HJ, United Kingdom*

[▽]*RIKEN Cluster for Pioneering Research, Wakoshi, Saitama, 351-0106, Japan*

^{††}*Department of Experimental Physics, Maynooth University, Maynooth, Co. Kildare W23 F2H6, Ireland*

^{‡‡}*Department of Physics and Astronomy, The University of Toledo, 2801 West Bancroft Street, Toledo, OH 43606, USA*

^{¶¶}*Jet Propulsion Laboratory, California Institute of Technology, 4800 Oak Grove Drive, Pasadena, CA 91109, USA*

E-mail: brunken@strw.leidenuniv.nl

Abstract

The evolution of interstellar ices can be studied with thermal tracers such as the vibrational modes of CO_2 ice that show great diversity depending on their local chemical and thermal environment. Now with the wide spectral coverage and sensitivity of the James Webb Space Telescope we can obtain observations of the weak and strong CO_2

absorption features inhabiting the near- and mid-infrared spectral region. In this work we present observations of the $15.2\ \mu\text{m}$ bending mode, the $4.39\ \mu\text{m}$ stretching mode and the $2.70\ \mu\text{m}$ combination mode of $^{12}\text{CO}_2$ and $^{13}\text{CO}_2$ ice in the high-mass protostar IRAS 20126 and the low-mass protostar Per-emb 35, two sources that show clear signs of ice heating. The $15.2\ \mu\text{m}$ bending mode of both protostars shows the characteristic double peak profile that is associated with pure CO_2 ice and a sharp short-wavelength peak is observed at $4.38\ \mu\text{m}$ in the $^{13}\text{CO}_2$ bands of the two sources. Furthermore, a narrow short-wavelength feature is detected at $2.69\ \mu\text{m}$ in the $^{12}\text{CO}_2$ combination mode of Per-emb 35. We perform a consistent profile decomposition on all three vibrational modes and show that the profiles of all three bands can be reproduced with the same linear combination of CO_2 ice in mixtures with mostly CH_3OH and H_2O ices when the ices undergo segregation due to heating. The findings show that upon heating, CO_2 ice is likely segregating from mostly the water-rich ice layer and the CO_2 - CH_3OH component becomes dominant in all three vibrational modes. Additionally, we find that the contribution of the different CO_2 components to the total absorption band is similar for both $^{12}\text{CO}_2$ and $^{13}\text{CO}_2$. This indicates that fractionation processes must not play a significant role during the different formation epochs, H_2O -dominated and CO -dominated, of the CO_2 ices and that ratio persists through the heating stage. We quantify the $^{12}\text{CO}_2$ and $^{13}\text{CO}_2$ ice column densities and derive $^{12}\text{C}/^{13}\text{C}_{\text{ice}} = 90 \pm 9$ in IRAS 20126, a value that is lower compared to what was previously reported for warm gaseous CO in this source. Finally, we report the detection of the $^{13}\text{CO}_2$ bending mode of pure CO_2 ice at $15.64\ \mu\text{m}$ in both IRAS 20126 and Per-emb 35.

Introduction

The formation of an infant star in a collapsing dark molecular cloud marks the beginning of the protostellar stage. These stellar cradles are also the formation sites of interstellar ices where the low temperatures and higher densities enable atoms and small molecules to stick to the surfaces of cold dust grains. These small species will subsequently react to create

the molecules that later evolve and become the prebiotic material that is incorporated into planets¹. Consequently, it is imperative to study the chemical journey of interstellar ices in order to define the initial conditions that could potentially lead to habitability. One process that can significantly alter the structure and composition of interstellar ices is heating by the central protostar^{2–6}. This thermal processing also alters the infrared absorption features of these ices, a well-known example being the crystalline profile of water ice⁷, and these ice absorption bands can therefore act as probes when examining physicochemical processes.

The vibrational modes of CO₂ ice in particular have been well studied for their ability to trace ice heating and composition^{8–15}. Studies have shown that both the 15.2 μm bending mode of ¹²CO₂^{11,12,14–17} and the 4.39 μm stretching mode of ¹³CO₂^{12,15} change dramatically depending on the line of sight. The 15.2 μm bending mode, for instance, is known to split into two peaks and the appearance of a second peak is observed at 4.38 μm in infrared spectra of luminous protostars. Both spectral features have been attributed to segregated CO₂ ice, a process in which CO₂ molecules cluster together and form inclusions of pure CO₂ ice in the otherwise mixed ice mantles upon protostellar heating^{5,9,14}.

The era of the James Webb Space Telescope (JWST) provides new and unique opportunities to study the vibrational modes of CO₂ ice at higher S/N in high-mass and solar-mass protostars. In particular, its exceptional sensitivity enables observations of weak features such as the 2.70 μm ¹²CO₂ combination mode and the 4.39 μm ¹³CO₂ stretching mode. These weaker bands have the additional advantage of being unsusceptible to the grain shape and size effects that can further alter the band profiles^{18–20}. Finally, the wide spectral coverage of the JWST allows access to the strong ¹²CO₂ 4.27 μm stretching mode and 15.2 μm bending mode^{15,21} enabling a complete study of all the CO₂ ice absorption features.

In this work we use JWST observations to investigate the environment of CO₂ ice in the low-mass-protostar Per-emb 35 and the high mass protostar IRAS 20126+4104 (hereafter IRAS 20126) as part of the JWST Observations of Young protoStars (JOYS+) program^{22–24} and the Investigating Protostellar Accretion Across the Mass Spectrum (IPA) program^{25–27}.

Both sources show spectral signatures of thermally processed ices. We perform for the first time a consistent profile decomposition of three $^{12}\text{CO}_2$ bands: the $^{12}\text{CO}_2$ ν_2 bending mode ($15.2\ \mu\text{m}$), the $^{13}\text{CO}_2$ ν_3 stretching mode ($4.39\ \mu\text{m}$) and the $\nu_1 + \nu_3$ combination mode ($2.70\ \mu\text{m}$). This paper is structured as follows. In Sect. 2 we present our observations and provide the methods used for the profile analysis. In Sect. 3 we present the spectral decompositions. The results are discussed in Sect. 4, and the main points of this work are summarized in Sect. 5.

Observations and Methods

Observations

The observations of Per-emb 35 were taken as part of the JOYS+ Cycle 1 NIRSpec program (PI: E.F. van Dishoeck, ID: 1960) and MIRI (PI: M. E. Ressler, ID: 1236) programs. The data consist of NIRSpec ($1 - 5\ \mu\text{m}$) spectra observed using the G235H and G395H modes ($R = \lambda / \Delta \lambda = 2700$) and MIRI ($5 - 28\ \mu\text{m}$) spectra observed using MIRI MRS gratings (A, B, and C). The IPA observations of IRAS 20126 were obtained as part of the IPA Cycle 1 GO program (PI: T.Megeath, ID: 1802) using the NIRSpec G395M mode ($R = \lambda / \Delta \lambda = 1000$) and MIRI MRS gratings. Both spectrometers are integral field units and the spectra were extracted centered on the infrared source using a $3\lambda/D$ cone aperture. We note that a circle aperture with fixed radius provides similar spectra as a cone aperture extraction. Absolute calibration errors are less than 5% for both instruments. Further observational details, data reduction methods, information on the spectral extractions coordinates and source properties are provided Table 6 and in references^{15,21,25,27–30}. An overview of the ice bands discussed in this work is presented in Figure 1 for Per-emb 35 and IRAS 20126.

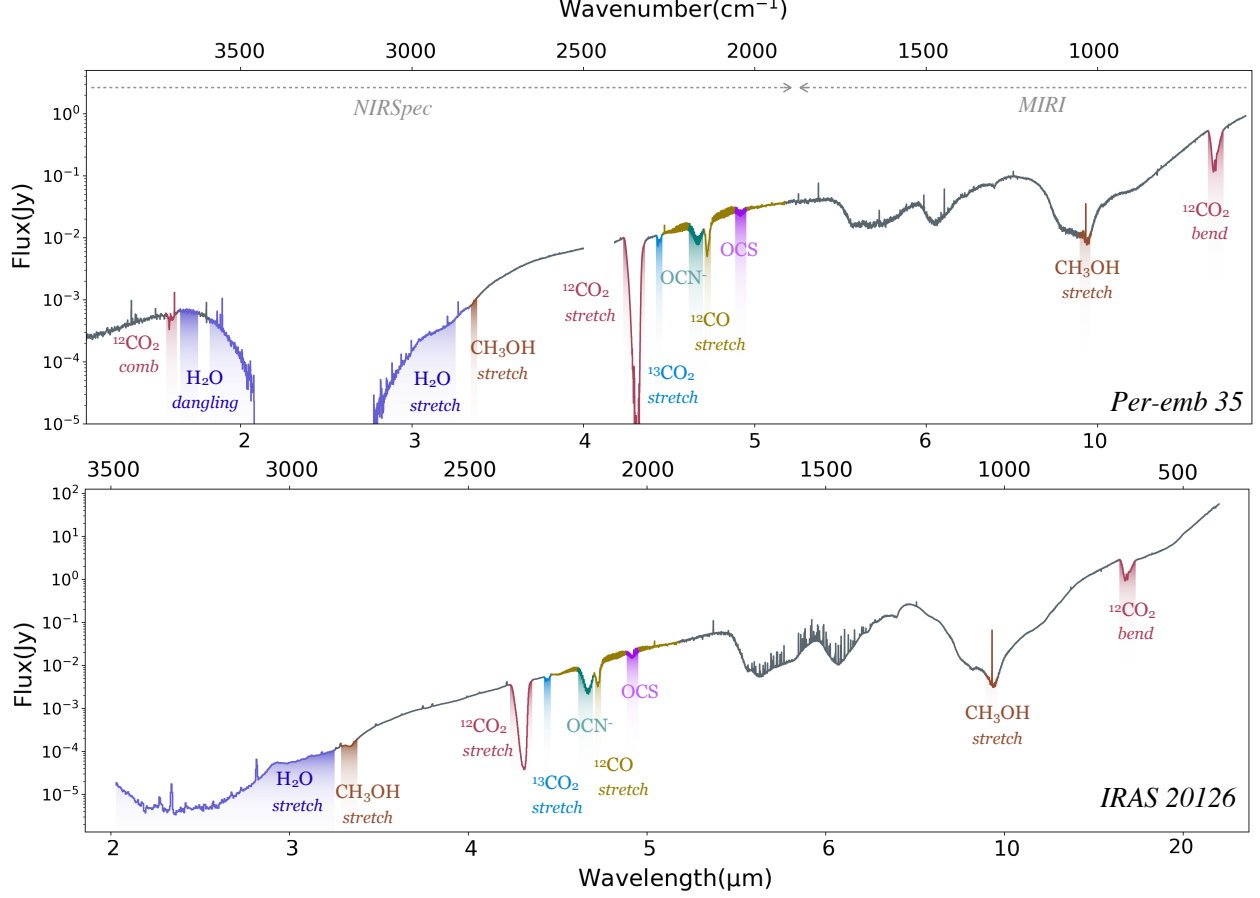


Figure 1: Full JWST NIRSpec and MIRI spectra for Per-emb 35 and IRAS 20126. The ice absorption features are shaded in color.

Continuum subtraction

For the continuum subtractions on the $2.70 \mu\text{m}$ band of Per-emb 35 and the $4.39 \mu\text{m}$ bands of Per-emb 35 and IRAS 20126, we first applied a local continuum over the ice bands and subsequently used this to convert the spectra from flux scale to optical depth scale using equation (1),

$$\tau_{\lambda}^{obs} = -\ln\left(\frac{F_{\lambda}^{obs}}{F_{\lambda}^{cont}}\right), \quad (1)$$

where F_{λ}^{obs} is the observed flux and F_{λ}^{cont} is the flux of the continuum. Further details on the continuum placement and the anchor points used in each spectral region are described

with supporting figures in Brunken et al.²¹.

The continuum in the 15 μm region was subtracted by first fitting a global continuum following the methods presented in Boogert et al.⁶, Poteet et al.³¹. After subtracting the continuum and converting the spectra to optical depth scale, we fitted the silicate template of GCS 3 to the 9.7 μm and 18 μm silicate features and subtracted this from the spectra³². The line of sight of GCS 3 passes through a large column density of a diffuse cloud containing silicates but little ices. Following the silicate subtraction we fitted laboratory data of water ice at various temperatures³³ to subtract the water libration mode at 12.6 μm from the spectrum of Per-emb 35. The continuum subtraction and water libration mode subtraction for Per-emb 35 are presented in Figures 7 and 8 in the Supporting Information section.

The spectrum of IRAS 20126 proved to be more difficult to fit with the water laboratory data currently available to us and we opted instead to fit a local continuum over the CO₂ 15.2 μm band to simulate the wing of the water libration mode and subtracted this from the spectrum. We note that this method of simulating the overlapping spectral features in this region with local continua and Gaussian curves is similar to the methods applied in Gerakines et al.¹¹ and Pontoppidan et al.¹⁴. The final spectra of IRAS 20126 are shown on optical depth scale in Figure 9. The uncertainty on the continuum placement can account for up to 20% in the error budget²¹.

Spectral decomposition

The spectral decompositions of the 2.70 μm , the 4.39 μm and the 15.2 μm bands of CO₂ were performed using laboratory spectra. The laboratory data^{8,10,34} that provided the best fit are presented in Table 1 and are publicly available on the Leiden Ice Data Base (LIDA)³⁵.

To correct for the grain shape and size effects that affect the strong vibrational mode at 15.2 μm ²⁰, we used `optool`³⁶ and performed corrections for a continuous distribution of

Table 1: Laboratory spectra.

Ice sample	Ratio	$T(K)$	Resolution (cm^{-1})	Reference
$\text{CO}_2:\text{H}_2\text{O}$	1:1	100	1	Ehrenfreund et al. ¹⁰
$\text{CO}_2:\text{CH}_3\text{OH}$	1:1	115	1	Ehrenfreund et al. ¹⁰
$\text{CO}_2:\text{CO}$	1:1	15	0.5	van Broekhuizen et al. ³⁴
$\text{CO}_2:\text{CO}$	1:2	25	0.5	van Broekhuizen et al. ³⁴
CO_2	Pure	80	1	Ehrenfreund et al. ⁸

ellipsoids (CDE) on the laboratory spectrum of pure CO_2 . These effects are negligible for the weaker vibrational mode at $2.70 \mu\text{m}$ and the $4.39 \mu\text{m}$ band of $^{13}\text{CO}_2$ because the isotopologue is diluted in $^{12}\text{CO}_2$. The particle shape effects are also negligible for the laboratory spectra where CO_2 is diluted in other species^{8,37}.

The bands were fitted using a χ^2 minimization routine that provides the best linear combination of five components each representative of CO_2 in a specific chemical environment¹⁴. The best fit was selected based on the lowest χ^2 value and for the components we used laboratory spectra of the binary ices $\text{CO}_2:\text{H}_2\text{O}$, $\text{CO}_2:\text{CH}_3\text{OH}$, $\text{CO}_2:\text{CO}$ and pure CO_2 ice. Given the number of mixing ratios available for each binary ice, we opted to use the mixing ratios determined in previous CO_2 studies^{14,15} as a starting point and introduced new mixing ratios when necessary. As input spectra for the χ^2 minimization routine, we used all available temperature measurements for a given mixing ratio.

The $15.2 \mu\text{m}$ band of IRAS 20126 was first fitted with the linear combination used in Brunken et al.¹⁵ to fit the $^{13}\text{CO}_2$ $4.39 \mu\text{m}$ band in this source. If this initial linear combination failed to reproduce the $15.2 \mu\text{m}$ band, the $4.39 \mu\text{m}$ band analysis was re-fitted with a combination of different laboratory spectra. For example, a new mixing ratio could be introduced before running the χ^2 routine to find a new best fit for the $4.39 \mu\text{m}$ feature. The $4.39 \mu\text{m}$ band analysis was re-visited because the components are better isolated and therefore more distinguishable in this vibrational mode compared to the $15.2 \mu\text{m}$ bending mode.

Once a new best fit was found for the $4.39 \mu\text{m}$ band, we ran the χ^2 routine with all the available temperatures of this new mixing ratio on the $15.2 \mu\text{m}$ band to test whether the

routine would select the same spectra to fit this feature. If the band was instead fitted with a different linear combination, we used the selected five spectra to fit the at 4.39 μm and test if this combination could also reproduce the $^{13}\text{CO}_2$ feature. If a spectrum in this combination failed to reproduce the 4.39 μm band, it was removed from the list of input spectra, and we ran the χ^2 routine again on the 15 μm band with the remaining input spectra. This process was repeated until consistent results were found between the bands, after which the 2.70 μm band was included in the analysis to expand the consistency check. The routine provides 1σ uncertainties on each fitted component. This is a margin for how much the contribution of each component can be increased or decreased before the band profile is no longer reproduced by the linear combination. This multi-band analysis allowed us to provide additional constraints on the components and lower some of the degeneracies between the laboratory spectra. Further details on the fitting of our sources are presented in the Analysis section.

Column densities

The column densities are calculated using equation 2:

$$N = \frac{\int \tau_\nu d\nu}{A}, \quad (2)$$

where $\int \tau_\nu d\nu$ is the integrated optical depths under the absorption feature, and A is the corresponding band strength of the vibrational mode. For the band strength we used the values determined by Gerakines et al.³⁸ and corrected by Bouilloud et al.³⁹. The corrected band strengths used in this work are presented Table 2. In order to facilitate comparison with studies that do not use the corrected band strengths, we have included the correction factors that can be used to convert the column densities. The column densities derived in this work need to be multiplied with these correction factors in order to compare them with column densities derived using the uncorrected band strengths.

Table 2: Band strengths of CO₂ ice.

Position (μm)	A (cm molecule ⁻¹)	Correction Factor	References
2.70	2.1×10^{-18}	1.4	Gerakines et al. ³⁸ (corrected)
4.27	1.1×10^{-16}	1.45	Gerakines et al. ³⁸ (corrected)
15.2	1.6×10^{-17}	1.45	Gerakines et al. ³⁸ (corrected)
4.39	1.15×10^{-16}	1.47	Gerakines et al. ³⁸ (corrected)

Notes. The corrected values of Gerakines et al.^{38,40} were taken from Bouilloud et al.³⁹. The column densities derived in this work can be multiplied by the correction factors to compare them with the values derived using the band strengths reported in Gerakines et al.³⁸ and Gerakines et al.⁴⁰.

Analysis

In the following sections we present the profile analysis of the ¹²CO₂ ν_2 bending mode (15.2 μm), the ¹³CO₂ ν_3 stretching mode (4.39 μm) and the ¹²CO₂ $\nu_1 + \nu_3$ combination mode (2.70 μm). The strong ¹²CO₂ ν_3 stretching mode at 4.27 μm is observed in both sources but is saturated ($\tau > 5$). Its true optical depth therefore remains uncertain. Furthermore, its profile is highly sensitive to grain shape and size effects^{19,20}. Consequently, we opted to exclude this band from this analysis. We also report the detection of a weak feature at 15.64 μm which we assign to the bending mode of ¹³CO₂ ice.

High-mass protostar: IRAS 20126

In Figure 2 we present the profile analysis of the 4.39 μm band of ¹³CO₂ and the 15.2 μm band of ¹²CO₂ in the high-mass source IRAS 20126. Currently there are no NIRSpect G235M observations of this source and the 2.70 μm combination mode is therefore not available.

Table 3: Fraction of integrated optical depth IRAS 20126

Component	Mixture	4.39 μm (%)	15.2 μm (%)
CO ₂ :H ₂ O	1:1	20 ± 10	18 ± 1
CO ₂ :CH ₃ OH	1:1	60 ± 2	58 ± 1
CO ₂ :CO	1:1	$1 \pm {}^{+6}_{-1}$	2 ± 1
CO ₂ :CO	1:2	$1 \pm {}^{+2}_{-1}$	2 ± 1
CO ₂	Pure	18 ± 2	21 ± 1

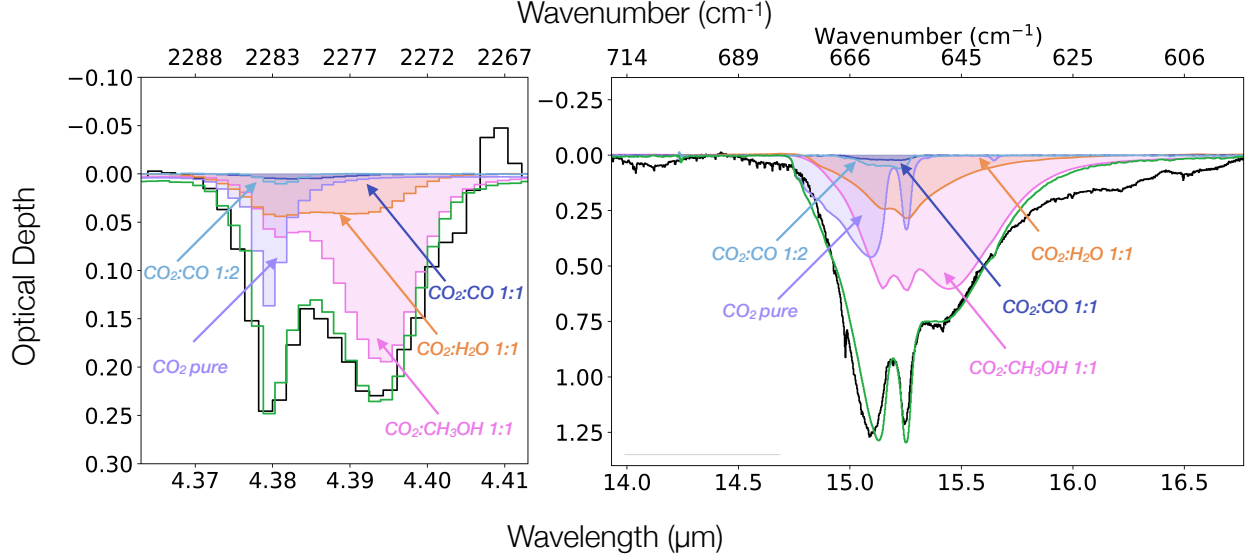


Figure 2: Band profile analysis of IRAS 20126. Left: Decomposition of the $4.39 \mu\text{m}$ $^{13}\text{CO}_2$ band. Right: Decomposition of the $15.2 \mu\text{m}$ $^{12}\text{CO}_2$ band. The purple, pink, orange, light blue and dark blue shaded areas correspond to the pure CO_2 80 K, $\text{CO}_2:\text{CH}_3\text{OH}$ 1:1 115 K, $\text{CO}_2:\text{H}_2\text{O}$ 1:1 100 K, $\text{CO}_2:\text{CO}$ 1:2 25 K and $\text{CO}_2:\text{CO}$ 1:1 15 K component, respectively. Finally the green line shows the sum of all the components. The poor fit at $16.2 \mu\text{m}$ and $16.5 \mu\text{m}$ is likely due to absorption features of crystalline silicates.

The $^{13}\text{CO}_2$ feature of IRAS 20126 was first modeled by Brunken et al.¹⁵, who performed a phenomenological decomposition of the ice feature and identified the peak positions and widths of three main components: a short-wavelength peak, a long-wavelength peak and a middle component (Supplementary Table 7). The band was subsequently fitted with a linear combination of five laboratory spectra based on the study by Pontoppidan et al.¹⁴ of the $15.2 \mu\text{m}$ bending mode. The components are representative of CO_2 ice in the following environments: pure CO_2 ice, CO_2 in an H_2O -rich environment, CO_2 mixed with CH_3OH , CO_2 diluted in CO and CO_2 mixed with CO in equal ratios. Brunken et al.¹⁵ compared the width and central positions of the short-wavelength, long-wavelength and middle component of the $4.39 \mu\text{m}$ band (Supplementary Table 7) with those of various laboratory spectra and selected five laboratory spectra to fit this absorption band: $\text{CO}_2:\text{H}_2\text{O}$ 1:10 10 K, $\text{CO}_2:\text{CH}_3\text{OH}$ 1:10 10 K, $\text{CO}_2:\text{CO}$ 1:1 15 K, $\text{CO}_2:\text{CO}$ 1:2 25 K and pure CO_2 80 K. For further details on this selection process, we refer the reader to Brunken et al.¹⁵.

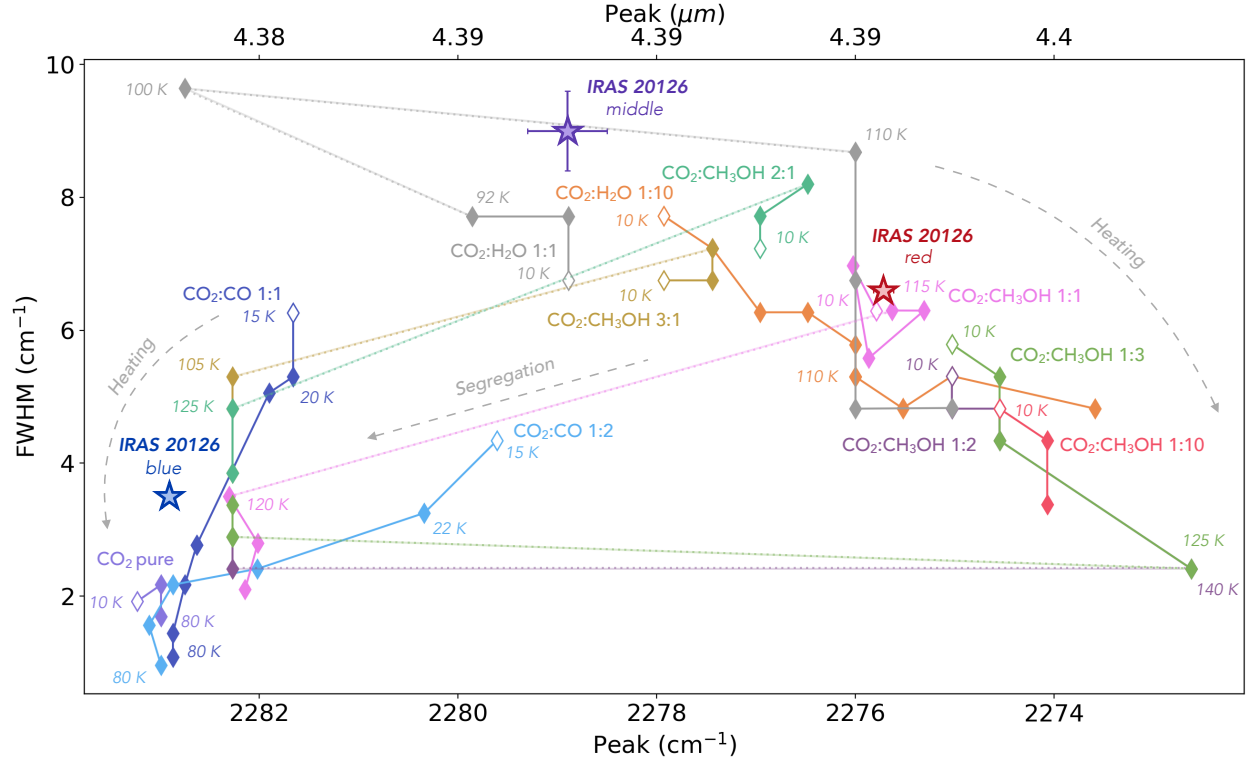


Figure 3: Full width at half maximum and peak positions of the available laboratory CO_2 spectra of the $4.39 \mu\text{m}$ $^{13}\text{CO}_2$ band. The arrows indicate how ice heating and segregation is affecting these quantities. The width and central positions measured for the long-wavelength, short-wavelength and middle components of the $^{13}\text{CO}_2$ band are shown as colored stars.

In Figure 3 we present an extended version of Figure 3 from Brunken et al.¹⁵ showing the evolution of the full width at half maximum (FWHM) and central positions of the available CO_2 laboratory spectra for the $4.39 \mu\text{m}$ band of $^{13}\text{CO}_2$. The widths and peak positions of the long-wavelength, short-wavelength and middle components measured for the $^{13}\text{CO}_2$ band in IRAS 20126 are also shown.

The $15.2 \mu\text{m}$ bending mode of IRAS 20126 was initially modeled using the same combination of laboratory spectra selected by Brunken et al.¹⁵ as a starting point. Given the susceptibility of the $15.2 \mu\text{m}$ band to grain shape and size effects, we applied a CDE correction on the laboratory spectrum of pure CO_2 prior to the fitting. This five-component linear combination failed to reproduce the $15.2 \mu\text{m}$ absorption band however because the laboratory spectrum of $\text{CO}_2:\text{CH}_3\text{OH}$ 1:10 at 10 K is too red-shifted to fit the shoulder located

at 15.4 μm . Laboratory spectra of $\text{CO}_2\text{:CH}_3\text{OH}$ 1:10 ices at higher temperatures also failed to reproduce this shoulder. Brunken et al.¹⁵ also provided an alternative three-component linear combination of solely heated ices but this failed to reproduce the 15.2 μm feature as well.

Consequently, we revisited the profile analysis of the $^{13}\text{CO}_2$ 4.39 μm band. The width and central position of the long-wavelength feature observed in the $^{13}\text{CO}_2$ band (Table 7) were compared to laboratory spectra of $\text{CO}_2\text{:CH}_3\text{OH}$ ices and the results indicate that the 1:1 mixing ratio produces bands with properties that coincide with this peak (Figure 3). The $\text{CO}_2\text{:CH}_3\text{OH}$ 1:10 laboratory spectra were then exchanged in favor of the 1:1 spectra and we ran the χ^2 fitting routine with these new input spectra as described in Section 2. Our findings show that the band profiles of both vibrational modes are successfully reproduced with the $\text{CO}_2\text{:CH}_3\text{OH}$ 1:1 spectrum at 115 K as shown in Figure 2.

While the $\text{CO}_2\text{:H}_2\text{O}$ 1:10 at 10 K successfully fitted both vibrational modes, the possibility of a warm $\text{CO}_2\text{:H}_2\text{O}$ component was also considered given that both the 15.4 μm shoulder and the 4.39 μm peak are better fitted with high-temperature $\text{CO}_2\text{:CH}_3\text{OH}$ spectra. Ice heating causes the $\text{CO}_2\text{:H}_2\text{O}$ 1:10 spectra to shift to significantly longer wavelengths however (Figure 3) and these spectra no longer fit the $^{13}\text{CO}_2$ band in a five-component linear combination. Therefore, we opted to run the χ^2 routine with spectra of $\text{CO}_2\text{:H}_2\text{O}$ ices in different mixing ratios. Given the limited available laboratory data, we selected the $\text{CO}_2\text{:H}_2\text{O}$ 1:1 mixture; the abundance of CO_2 with respect to H_2O is $\sim 20 - 50\%$ in the protostellar envelopes².

Figure 2 shows that the band profiles of both the $^{13}\text{CO}_2$ 4.39 μm and the $^{12}\text{CO}_2$ 15.2 μm bands are successfully fitted with high-temperature spectra of this 1:1 mixing ratio. The Supplementary Figure 10 shows the alternative fit with the cold $\text{CO}_2\text{:H}_2\text{O}$ 1:10 spectrum at 10 K. Thus, there is a clear degeneracy between these $\text{CO}_2\text{:H}_2\text{O}$ laboratory spectra. In the Discussion section we will argue why the high-temperature water spectra are better suited for the analysis of the vibrational modes in IRAS 20126 and Per-emb 35.

In Table 3 we present the fraction of each component with respect to the total integrated

optical depth including their 1σ uncertainties. The fraction of integrated optical depth is consistent between the two bands within these uncertainties. The χ^2 for the $4.39\ \mu\text{m}$ and $15.2\ \mu\text{m}$ bands are 2.8 and 3.0, respectively. It is worth noting that the contribution of these components remains the same when the $\text{CO}_2\text{:H}_2\text{O}$ 1:1 100 K spectrum is exchanged for the 1:10 mixture at 10 K.

Finally, Figure 2 shows that the long-wavelength wing of the bending mode is poorly fitted above $15.8\ \mu\text{m}$. In particular, there are two notable features at $16.2\ \mu\text{m}$ and $16.5\ \mu\text{m}$ that we were unable to reproduce with the laboratory data. These could be absorption features of crystalline silicates such as forsterite and enstatite. Additional evidence of these crystalline silicates was found at longer wavelengths with detections of the characteristic absorption band of crystalline forsterite at $23.2\ \mu\text{m}$ ⁴¹ but these features could also be present at shorter wavelengths. Removing these bands however requires a careful modeling of all the silicates features spanning the $9 - 27\ \mu\text{m}$ spectral region and this is beyond the scope of this paper.

Low mass protostar: Per-emb 35

After successfully fitting the two absorption features of IRAS 20126, we applied the linear combination to the ice absorption bands of the low-mass protostar Per-emb 35. This source is particularly interesting to study because the $^{12}\text{CO}_2$ combination mode located at $2.70\ \mu\text{m}$ is observed with the NIRSpect G235H mode. The three CO_2 vibrational modes in Per-emb 35 are successfully fitted with the same linear combination, the results are presented in Figure 4. The contribution of each individual component with respect to the total absorption is presented in Table 4. These fractions are consistent between the three bands within the reported uncertainties and are also similar to the fractions derived in IRAS 20126. The alternative analysis with cold $\text{CO}_2\text{:H}_2\text{O}$ ice is shown in Supplementary Figure 11.

The sharp short-wavelength feature observed at $4.38\ \mu\text{m}$ is successfully fitted with the laboratory spectrum of pure CO_2 ice at 80 K. The pure CO_2 80 K spectrum also reproduces

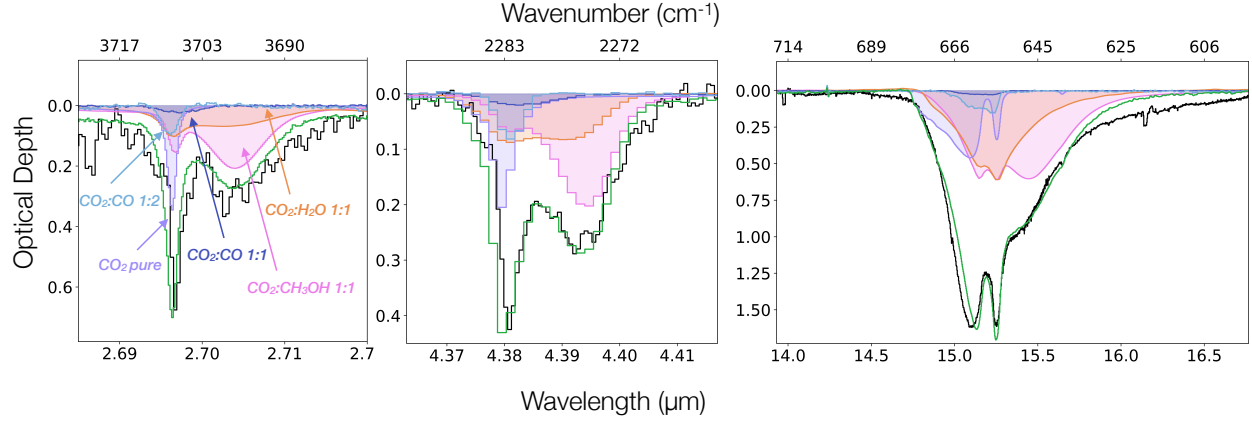


Figure 4: Band profile analysis of Per-emb 35. Left: Decomposition of the $2.70 \mu\text{m}$ $^{12}\text{CO}_2$ band. Middle: Decomposition of the $4.39 \mu\text{m}$ $^{13}\text{CO}_2$ band. Right: Decomposition of the $15.2 \mu\text{m}$ $^{12}\text{CO}_2$ band. The purple, pink, orange, light blue and dark blue shaded areas correspond to the pure CO_2 80 K, $\text{CO}_2:\text{CH}_3\text{OH}$ 1:1 115 K, $\text{CO}_2:\text{H}_2\text{O}$ 1:1 100 K, $\text{CO}_2:\text{CO}$ 1:2 25 K and $\text{CO}_2:\text{CO}$ 1:1 15 K component, respectively. Finally the green line shows the sum of all the components.

the short-wavelength peak observed at $2.69 \mu\text{m}$ in the $^{12}\text{CO}_2$ combination mode as well as the split peak profile in the bending mode at $15.2 \mu\text{m}$. This pure CO_2 component is typically $\sim 15 - 20\%$ of the total integrated optical depth in both IRAS 20126 and Per-emb 35 and the strong contribution of this component indicates that these ices are undergoing segregation. The χ^2 value for the fittings of the $2.70 \mu\text{m}$, $4.39 \mu\text{m}$ and $15.2 \mu\text{m}$ bands are 7.54, 0.2 and 5.9, respectively.

Table 4: Fraction of integrated optical depth Per-emb 35

Component	mixture	$2.70 \mu\text{m}$ (%)	$4.39 \mu\text{m}$ (%)	$15.2 \mu\text{m}$ (%)
$\text{CO}_2:\text{H}_2\text{O}$	1:10	28 ± 4	28 ± 9	31 ± 1
$\text{CO}_2:\text{CH}_3\text{OH}$	1:1	50 ± 3	44 ± 1	47 ± 1
$\text{CO}_2:\text{CO}$	1:1	3 ± 3	4^{+6}_{-4}	1 ± 1
$\text{CO}_2:\text{CO}$	1:2	6 ± 6	6 ± 2	4 ± 1
CO_2	Pure	14 ± 3	19 ± 7	17 ± 1

We note that the contribution of $\text{CO}_2\text{-CO}$ mixed ices, previously inferred to be present for cold sources¹⁴, is very small in both IRAS 20126 and Per-emb 35. This lack of CO ice

is however consistent with the weak ^{12}CO ice absorption band observed at $4.67\ \mu\text{m}$ in both sources and the strong rotation-vibrational lines of gaseous CO seen in the $4\ \mu\text{m}$ region of their spectra (Figure 1). In cold sources the $4.67\ ^{12}\text{CO}\ \mu\text{m}$ ice band is strong and often saturated ($\tau > 6$) and there is usually no strong OCN^- ice feature at $4.60\ \mu\text{m}$ ^{13,21}. In contrast, the $4.67\ \mu\text{m}$ CO ice band in IRAS 20126 has a peak optical depth of $\tau \sim 1.3$. This is relatively small compared to the strong OCN^- feature observed in this source ($\tau \sim 1.45$)²⁷. Similarly, the $4.67\ \mu\text{m}$ band in Per-emb 35 has a peak optical depth of $\tau \sim 1.3$ and has a strong OCN^- band of $\tau \sim 0.7$ (Figure 1). These spectral features all point towards thermal desorption of the bulk of the CO ice. The CO_2 -CO components are also more degenerate due to their complete overlap with the other components and as a result they also have the largest relative uncertainties.

The bending mode of $^{13}\text{CO}_2$ ice

A weak feature is observed at $15.64\ \mu\text{m}$ overlaid on the long-wavelength wing of the bending mode. We detect this feature in both IRAS 20126 and Per-emb 35 (Figure 5). The small absorption band is also observed in the laboratory spectrum of pure CO_2 leading us to conclude that this feature is likely the bending mode of $^{13}\text{CO}_2$.

This band is only clearly visible in the spectrum of pure CO_2 ice likely because it produces sharp narrow features as can be seen at $2.69\ \mu\text{m}$, $4.38\ \mu\text{m}$ and $15.2\ \mu\text{m}$. When CO_2 is diluted in other ices such as H_2O and CH_3OH this band probably becomes shallower and broader and therefore more difficult to detect. Because the $^{13}\text{CO}_2$ bending mode feature is small and there is a large uncertainty on the continuum needed to isolate it from the main $^{12}\text{CO}_2$ ice band, we refrain from doing further quantitative analysis on this feature in this work.

$^{12}\text{C}/^{13}\text{C}$

We quantified $^{12}\text{CO}_2$ and $^{13}\text{CO}_2$ column densities from the $15.2\ \mu\text{m}$ and $4.39\ \mu\text{m}$ features, respectively, and derived $^{12}\text{C}/^{13}\text{C} = 90 \pm 9$ in IRAS 20126. The $^{12}\text{CO}_2$ and $^{13}\text{CO}_2$ column

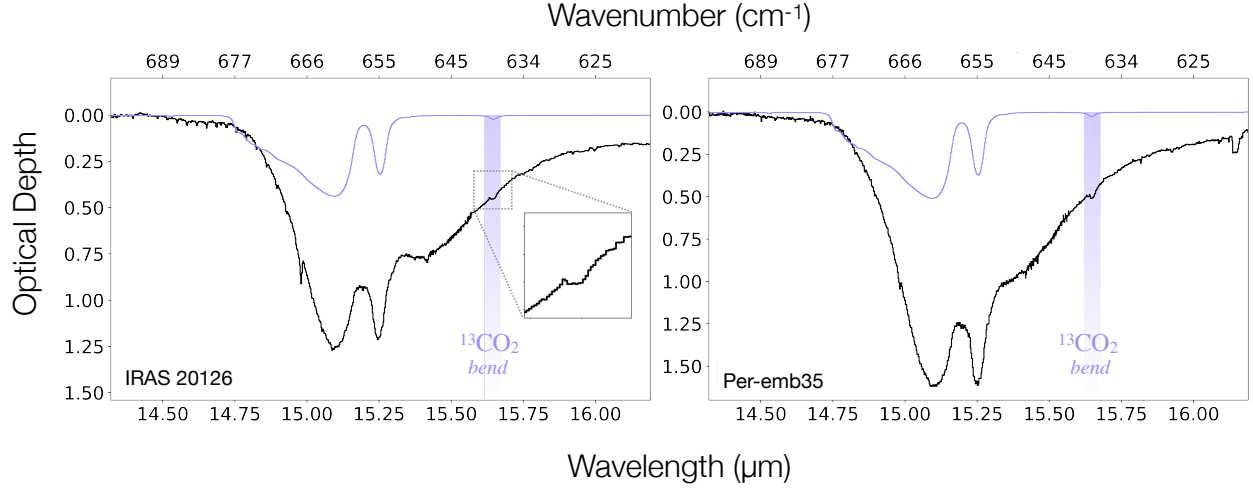


Figure 5: Bending mode of $^{13}\text{CO}_2$ ice. The $15.2\ \mu\text{m}$ bending of $^{12}\text{CO}_2$ is shown on optical depth scale (black) and the purple shaded column shows the absorption feature overlaid on the wing of the band at $15.64\ \mu\text{m}$. The purple line shows the laboratory spectrum of pure CO_2 at 80 K with a small absorption feature centered at $15.64\ \mu\text{m}$.

densities in Per-emb 35 were measured from the $2.70\ \mu\text{m}$ band, the $4.39\ \mu\text{m}$ band and the $15.2\ \mu\text{m}$ by Brunken et al.²¹ and the $^{12}\text{C}/^{13}\text{C}$ ratio derived for the $2.70\ \mu\text{m}$ combination mode and the $15.2\ \mu\text{m}$ bending mode are 132 and 99, respectively.

The observational errors are small, $\sim 10\%$ and the error uncertainty due to the continuum are up to $\sim 20\%$. The majority of the error budget, not included in the above error margins, comes from the uncertainties on the band strengths and can be up to $\sim 46\%$. For further details on the error analysis we refer the reader to Brunken et al.²¹. The findings are summarized in Table 5.

The $^{12}\text{C}/^{13}\text{C}_{ice} = 90 \pm 9$ measured in IRAS 20126 is consistent with the ratios measured from the CO_2 vibrational modes by Brunken et al.²¹ in the envelopes of low-mass protostars (their Table 5, mean ratio measured from the $15.2\ \mu\text{m}$ bending modes $\sim 97 \pm 17$). It is slightly elevated with respect to the ratio measured for the ISM $\sim 68^{12}$. This value is at the lower end of the gas-phase ratio previously measured in this same source by Rubinstein et al.²⁷ from hot gaseous CO rotation-vibrational lines $^{12}\text{C}/^{13}\text{C}_{gas} > 106$.

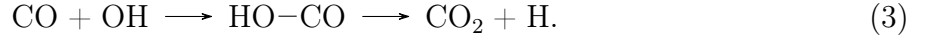
Table 5: $^{12}\text{CO}_2$ and $^{13}\text{CO}_2$ ice column densities in cm^{-2} .

Source	N $^{12}\text{CO}_2$ 2.70 μm	N $^{13}\text{CO}_2$ 4.39 μm	N $^{12}\text{CO}_2$ 15.2 μm	$^{12}\text{C}/^{13}\text{C}$ 2.70 μm	$^{12}\text{C}/^{13}\text{C}$ 15.2 μm
IRAS 20126	-	2.3×10^{16}	2.1×10^{18}	-	90 ± 9
Per-emb 35	3.7×10^{18}	2.8×10^{16}	2.8×10^{18}	132 ± 13	99 ± 10

Discussion

Formation and segregation of CO_2 ice

CO_2 chemistry occurs during both the H_2O -dominated phase and the CO -dominated phase of interstellar ice formation¹². The first formation route is facilitated by the formation of the HO-CO complex through the radical reaction^{5,42,43}:



The $\text{CO}_2\text{-H}_2\text{O}$ ices that ensue from this reaction are observed in all the vibrational modes of CO_2 ^{11,12,14,15,21} and are part of the polar H_2O -rich ice layer that forms during the translucent cloud phase when atomic H is abundant.

Apolar $\text{CO}_2\text{-CO}$ ices subsequently encapsulate the water-rich ice layer during the catastrophic CO freeze-out epoch⁴⁴ when OH reacts with CO on the cold grains. The high densities and low temperatures during this stage make it possible for CO to freeze out in large amounts on the dust grains spawning these CO-rich apolar ices. Additionally, the freeze-out also triggers the formation of molecules that use CO as feedstock such as methanol (CH_3OH), another key ingredient in interstellar ices⁴⁵ and a molecule that is known to be intimately mixed with CO_2 ^{9–12,14,15,21}.

When the young protostar heats its surrounding envelope, the most volatile species, including CO ice, sublime from the grains^{5,14} as illustrated in Figure 6. This CO desorption is evident in IRAS 20126 and Per-emb 35 from the weak CO ice band at 4.67 μm and the strong gaseous CO line-forest spanning the 4 μm spectral region^{15,21}. This distillation process

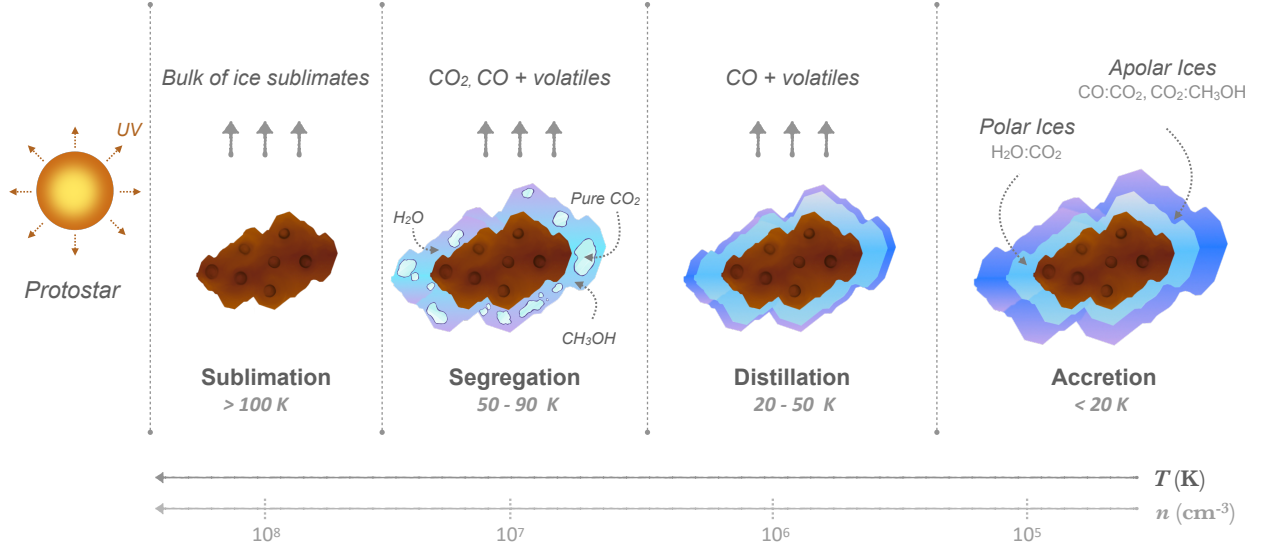


Figure 6: Schematic overview of CO_2 ice segregation in protostellar envelopes. The temperature and density zones are separated by the gray dashed lines and each grain represents a different stage of ice processing. Observations probe the entire line of sight from the central regions around the protostar to the outer envelope.

is also consistent with the experimental results from Ehrenfreund et al.⁹ who showed that above ~ 50 K H_2O , CO_2 and CH_3OH become the dominant species in interstellar ice spectra.

After distillation, segregation of CO_2 quickly follows as temperatures continue to rise in the envelope. During this segregation, the water molecules will rearrange and form links through hydrogen bonds. The new spatial proximity will allow the CO_2 molecules to cluster together and form bonds, producing inclusions of pure CO_2 ice inside the ice mantle¹⁰ (Figure 6). Because water desorbs at a much higher temperature than CO_2 , the pure CO_2 ice will remain trapped on the grain well beyond its desorption temperature. This multilayer formation mechanism coupled with the physicochemical processes that follow after, produce the different components that constitute the ice absorption bands observed in protostellar spectra. These absorption features include not only the components that are present on individual dust grains, but also the absorption of all the ices along the line sight. This extends from the hot central regions, to the ices in the colder outer envelope⁹ (Figure 6). Envelopes that are exposed to higher levels of protostellar heating, such as those around luminous protostars, have higher overall temperature and thus experience higher degrees of

ice processing.

The segregation of pure CO₂ ice is corroborated by the profile analyses done on the absorption bands in IRAS 20126 and Per-emb 35. Figures 2 and 4 show that a pure CO₂ component is observed in all the vibrational modes of CO₂ that accounts for up to $\sim 20\%$ of the total absorption band. At 2.69 μm and 4.38 μm this pure CO₂ ice component creates a narrow secondary absorption feature on the short-wavelength side of the bands. At 15.2 μm pure CO₂ ice produces the characteristic double peak structure. These features are not detected in the spectra of non-heated sources^{15,21}.

Another intrinsic feature of ice segregation is the deep shoulder observed at 15.4 μm that is associated with CO₂-CH₃OH ices^{9,46}. This shoulder is caused by the acid-base interaction between the carbon atom of CO₂ and the hydrogen atom of CH₃OH. Ehrenfreund et al.⁹ and Dartois et al.⁴⁶ both demonstrated with experimental studies that segregation is vital for the appearance of this shoulder which becomes observable in laboratory spectra with temperatures ranging between 65 K - 110 K. Many astronomical observations also support these findings, with numerous detections of this feature in high-mass and luminous protostars⁴⁶ including several massive young stellar objects populating the Central Molecular Zone (CMZ) ($R_{gal} < 200 \text{ pc}$)⁴⁷.

This shoulder is well fitted with a laboratory mixture of CO₂:CH₃OH 1:1 ice at 115 K (Figures 2 and 4). This is consistent with the temperature range reported in Dartois et al.⁴⁶ and the findings in Ehrenfreund et al.⁹ who showed that astronomical data are better fitted with 1:1 laboratory mixtures. The CO₂:CH₃OH 1:1 at 115 K spectrum also successfully reproduces the long-wavelength absorption features observed at 2.70 μm and 4.39 μm .

The values presented in Tables 3 and 4 show that fractions of integrated optical depths are similar within reported error margins. From these results it can be inferred that the ¹²C/¹³C ratios are also similar among the different ice components. This indicates that the carbon isotope ratio is likely set at the formation stage of the different CO₂ ices and that fractionation processes such as isotope exchange reactions^{48–50} appear to not have played a significant role

during neither the water-dominated phase nor the heavy CO freeze-out stage that produce the $\text{CO}_2\text{:H}_2\text{O}$ and $\text{CO}_2\text{:CH}_3\text{OH}$ ices. This ratio persists throughout the heating stage that produces the pure CO_2 component. We note however that this conclusion is drawn solely on the similarity between these fractions and that the isotope ratios have not been calculated for these individual components due to lack of experimental data. To the best of our knowledge there are currently no band strengths for $\text{CO}_2\text{:CH}_3\text{OH}$ mixtures for instance and band strengths measured at different temperatures are also limited. Quantifying the carbon isotope ratio for these individual components will therefore result in large uncertainties²¹.

Tables 3 and 4 and Figures 2 and 4 show that $\text{CO}_2\text{:CH}_3\text{OH}$ ices are the main contributors of the CO_2 vibrational modes. This conclusion differs from the findings presented in Pontoppidan et al.¹⁴ that fitted the $15.2\ \mu\text{m}$ bands with mostly with $\text{CO}_2\text{-H}_2\text{O}$ ices. Our results also differ from the analysis presented in Slavicinska et al.³³ who fitted the $3.5\ \mu\text{m}$ CH_3OH band in IRAS 20126 with mostly $\text{CH}_3\text{OH:H}_2\text{O}$ and pure CH_3OH ices and found no contribution of $\text{CO}_2\text{:CH}_3\text{OH}$ ices. These differences are discussed in the following section.

$\text{CO}_2\text{-CH}_3\text{OH}$ vs. $\text{CO}_2\text{-H}_2\text{O}$ ices

In contrast to the analysis presented in Pontoppidan et al.¹⁴ our results suggest that the $\text{CO}_2\text{:CH}_3\text{OH}$ component accounts for more than 40% of the three CO_2 vibrational modes in both IRAS 20126 and Per-emb 35. To understand the source of this difference, we revisited the band profile analysis and fitted the $15.2\ \mu\text{m}$ absorption features of IRAS 20126 and Per-emb 35 with the components used in Pontoppidan et al.¹⁴. The results indicate that the water component remains dominant in this particular linear combination because Pontoppidan et al.¹⁴ simulated the $15.4\ \mu\text{m}$ shoulder with a combination of two Gaussian curves. However, these Gaussian profiles only model the long-wavelength component of the $\text{CO}_2\text{:CH}_3\text{OH}$ ices centered at $15.4\ \mu\text{m}$. The short wavelength component located at $15.2\ \mu\text{m}$, which appears in all laboratory spectra of $\text{CO}_2\text{:CH}_3\text{OH}$ ices¹⁰, are not included in this model. As a result, the isolated long-wavelength feature creates a sharp shoulder that remains detectable in the

spectrum even when the contribution of the $\text{CO}_2\text{:H}_2\text{O}$ component greatly exceeds that of the $\text{CO}_2\text{:CH}_3\text{OH}$ component.

In contrast, when laboratory spectra of $\text{CO}_2\text{:CH}_3\text{OH}$ ices, containing both long- and short-wavelength components, are used, this shoulder becomes shallower in the final linear combination. This in turn will require a larger contribution from the $\text{CO}_2\text{:CH}_3\text{OH}$ ice to reproduce the shoulder and a smaller contribution from the $\text{CO}_2\text{:H}_2\text{O}$ component to avoid overfitting the band. Moreover, the short-wavelength component in the $\text{CO}_2\text{:CH}_3\text{OH}$ laboratory spectra also constrains the contribution of the pure CO_2 component at $15.2\text{ }\mu\text{m}$ since a balance between the two components is needed to avoid overproducing the double peak feature.

To confirm that this large fraction of $\text{CO}_2\text{:CH}_3\text{OH}$ ices is indeed caused by segregation, the ice absorption bands of two cold sources in the JOYS+ sample, Per-emb55-a and EDJ183-a, were also fitted. The results showed that the CO_2 ice bands in these cold sources have inherently larger fractions of $\text{CO}_2\text{:H}_2\text{O}$ ices. The band profile analysis presented in Brunken et al.¹⁵ also shows a large contribution of $\text{CO}_2\text{:H}_2\text{O}$ ices in the $^{13}\text{CO}_2$ bands of cold protostars. The small contribution of this component in our heated protostars therefore indicates that segregation must be occurring for the most part in the H_2O -rich ice layer. If so, then these $\text{CO}_2\text{:H}_2\text{O}$ ices should be both heated and showing signs of ice segregation. This is supported by the analysis where $\text{CO}_2\text{:H}_2\text{O}$ 1:1 spectra at 100 K are used to fit CO_2 ice features. Not only are there clear signs of ice segregation in the 1:1 mixture between 90 - 120 K with the appearance of the pure CO_2 peak at $4.38\text{ }\mu\text{m}$ (Figure 3), but this temperature range is also consistent with the temperature range of the $\text{CO}_2\text{:CH}_3\text{OH}$ component (115 K). Experimental results by He et al.⁵¹ also show that CO_2 needs to account for at least 23% of the ice mixture for segregation to take place, making the $\text{CO}_2\text{:H}_2\text{O}$ 1:1 spectrum a more appropriate choice for fitting the ice bands than the 1:10 mixture. While we do expect to have some contribution of cold ices in the outer envelope, the spectral features in both IRAS 202126 and Per-emb 35 indicate that the majority of the ices must be heated. Slavicinska et al.³³ for instance

showed that the 3 μm H_2O band of IRAS 20126 has a crystalline profile. We reiterate that exchanging the cold $\text{CO}_2\text{:H}_2\text{O}$ spectrum for the warm $\text{CO}_2\text{:H}_2\text{O}$ spectrum does not change the fractions of integrated optical depths. An intriguing question for future investigation is whether the total abundance of $\text{CO}_2\text{:H}_2\text{O}$ ices in cold sources equals the sum of the segregated pure CO_2 ice and the remaining $\text{CO}_2\text{:H}_2\text{O}$ ices in heated sources.

Regarding the CH_3OH 3.5 μm band in IRAS 20126, where Slavicinska et al.³³ showed that the feature is a composite of mostly pure CH_3OH ice and $\text{CH}_3\text{OH:H}_2\text{O}$ ices, the differences could be due to different ways of fitting and subtracting the continuum over the 3.5 μm CH_3OH band. This weak band is overlaid on the wing of the 3 μm water band whose shape is highly susceptible to grain shape and size effects. This introduces an uncertainty on the actual shape of the continuum. Dartois and d’Hendecourt⁵² for instance showed that the wing of the water band can be significantly raised with respect to the absorption feature at 3.5 μm . To test this, we revisited this band and raised the continuum over this region as shown in the left panel of Figure 12. The results indicate that $\text{CO}_2\text{:CH}_3\text{OH}$ can contribute significantly to this band if we use this approach (Figure 12, right panel). Additionally, prior to the analysis, PAH features peaking in this spectral region had to be removed which further adds to the uncertainties on the 3.5 μm feature. For the PAH removal, we followed the methods described Slavicinska et al.³³. Finally, we note that the 3.5 μm band overlaps with absorption features of ammonia hydrates that also peak at these wavelengths⁵³.

Conclusions

We present band profile analyses of the $^{12}\text{CO}_2$ 15.2 μm bending mode, the $^{13}\text{CO}_2$ 4.39 μm stretching mode and the $^{12}\text{CO}_2$ 2.70 μm combination mode that use a consistent set of laboratory ice mixtures in the high mass protostar IRAS 20126 and the low mass protostar Per-emb 35. The spectra of both sources show clear signs that the ices in the envelope are being heated by the central protostar prompting segregation of pure CO_2 ice.

- The 15.2 μm double peak feature and the short-wavelength features at 2.69 μm and 4.38 μm are successfully fitted with laboratory spectra of pure CO_2 ice at 80 K pointing towards segregation due to protostellar heating. This pure CO_2 component accounts for $\sim 20\%$ of the total absorption and is consistent across all the vibrational modes and between the low-mass and the high mass-protostar.
- The deep shoulder observed at 15.4 μm is reproduced the laboratory spectrum of $\text{CO}_2\text{:CH}_3\text{OH}$ 1:1 ices at 115 K. This spectrum also fitted the long-wavelength features at 2.70 μm in Per-emb 35 and 4.39 μm in both sources. This $\text{CO}_2\text{:CH}_3\text{OH}$ component is dominant in all the vibrational modes and accounts for more than 40% of the total band absorption. This is contrary to what has been previously observed in the CO_2 bands of non-heated sources where the $\text{CO}_2\text{:H}_2\text{O}$ ices are the main contributor. This indicates that CO_2 is likely segregating from mostly the water-rich ice layer.
- The contribution of each component with respect to the total integrated optical depth is similar in all the vibrational modes. This suggests that the $^{12}\text{C}/^{13}\text{C}$ ratio is already set at the formation stage of the different CO_2 ices and that fractionation processes did not play a significant role.
- We report the detection of the bending mode of $^{13}\text{CO}_2$ ice at 15.64 μm . The feature is overlaid on the long-wavelength wing of the $^{12}\text{CO}_2$ 15.2 μm band.
- We quantified the column densities and derived a $^{12}\text{C}/^{13}\text{C}_{ice} \sim 90$ in IRAS 20216. This value is slightly higher compared to the value measured for the ISM and lower than the gas-phase ratio recently derived for IRAS 20126. The $^{12}\text{C}/^{13}\text{C}_{ice}$ of Per-emb 35 was previously measured to be ~ 99 and ~ 132 for the 15.2 μm bending mode and the 2.70 μm combination mode, respectively, consistent with the values measured for other low mass sources. The observational uncertainties are $\sim 10\%$.

The findings in this work indicate that segregation dramatically changes the structure of these ices and that this process occurs in a similar manner in both the high-mass and the

low-mass protostar. Future work should investigate whether the total abundance of $\text{CO}_2\text{:H}_2\text{O}$ ices in non-heated sources matches the sum of the segregate pure CO_2 ice and the remainder of the $\text{CO}_2\text{:H}_2\text{O}$ ices in heated sources. Furthermore, more laboratory data of CO_2 band strengths are needed, in particular band strengths were CO_2 is mixed with other ices, such as CH_3OH , as well as band strengths measured at different temperatures. These measurements are crucial to accurately determine the column density of these ices and the carbon isotope ratio. Finally, since CO_2 and H_2O ice are originally intimately mixed, additional laboratory data with new more mixing ratios are needed to better study the chemical evolution of this component in both heated and cold sources.

Acknowledgement

The lead authors have had the pleasure of working closely with Prof. Harold Linnartz for many years on interstellar ices, combining his work in the Laboratory for Astrophysics with astronomical observations. The spectroscopy and chemistry of CO_2 ice has been a focus of his research in Leiden and this work is therefore a salute to his contributions to Astrochemistry. Astrochemistry in Leiden is supported by the Netherlands Research School for Astronomy (NOVA), by funding from the European Research Council (ERC) under the European Union’s Horizon 2020 research and innovation programme (grant agreement No. 101019751 MOLDISK. Support by the Danish National Research Foundation through the Center of Excellence “InterCat” (Grant agreement no.: DNR150) is also acknowledged. This work is based on observations made with the NASA/ESA/CSA James Webb Space Telescope. The data were obtained from the Mikulski Archive for Space Telescopes at the Space Telescope Science Institute, which is operated by the Association of Universities for Research in Astronomy, Inc., under NASA contract NAS 503127 for JWST. The following National and International Funding Agencies funded and supported the MIRI development: NASA; ESA; Belgian Science Policy Office (BELSPO); Centre Nationale d’Etudes Spatiales

(CNES); Danish National Space Centre; Deutsches Zentrum für Luft und Raumfahrt (DLR); Enterprise Ireland; Ministerio De Economía y Competitividad; Netherlands Research School for Astronomy (NOVA); Netherlands Organisation for Scientific Research (NWO); Science and Technology Facilities Council; Swiss Space Office; Swedish National Space Agency; and UK Space Agency.

References

- (1) van Dishoeck, E. F. Astrochemistry of dust, ice and gas: introduction and overview. *Faraday Discussions* **2014**, *168*, 9.
- (2) Boogert, A. C. A.; Gerakines, P. A.; Whittet, D. C. B. Observations of the icy universe. *Annu. Rev. Astron. Astrophys.* **2015**, *53*, 541–581.
- (3) Cuppen, H. M.; Linnartz, H.; Ioppolo, S. Laboratory and Computational Studies of Interstellar Ices. *Annu. Rev. Astron. Astrophys.* **2024**, *62*, 243–286.
- (4) Visser, R.; van Dishoeck, E. F.; Doty, S. D.; Dullemond, C. P. The chemical history of molecules in circumstellar disks. I. Ices. *Astron. Astrophys.* **2009**, *495*, 881–897.
- (5) Öberg, K. I.; Boogert, A. C. A.; Pontoppidan, K. M.; van den Broek, S.; van Dishoeck, E. F.; Bottinelli, S.; Blake, G. A.; Evans, I., Neal J. The Spitzer Ice Legacy: Ice Evolution from Cores to Protostars. *Astrophys. J.* **2011**, *740*, 109.
- (6) Boogert, A. C. A. et al. The c2d Spitzer Spectroscopic Survey of Ices around Low-Mass Young Stellar Objects. I. H₂O and the 5–8 μ m Bands. *Astrophys. J.* **2008**, *678*, 985–1004.
- (7) Fraser, H. J.; Collings, M. P.; McCoustra, M. R. S.; Williams, D. A. Thermal desorption of water ice in the interstellar medium. *Mon. Not. R. Astron. Soc.* **2001**, *327*, 1165–1172.

- (8) Ehrenfreund, P.; Boogert, A. C. A.; Gerakines, P. A.; Tielens, A. G. G. M.; van Dishoeck, E. F. Infrared spectroscopy of interstellar apolar ice analogs. *Astron. Astrophys.* **1997**, *328*, 649–669.
- (9) Ehrenfreund, P.; Dartois, E.; Demyk, K.; D’Hendecourt, L. Ice segregation toward massive protostars. *Astron. Astrophys.* **1998**, *339*, L17–L20.
- (10) Ehrenfreund, P.; Kerkhof, O.; Schutte, W. A.; Boogert, A. C. A.; Gerakines, P. A.; Dartois, E.; D’Hendecourt, L.; Tielens, A. G. G. M.; van Dishoeck, E. F.; Whittet, D. C. B. Laboratory studies of thermally processed H₂O-CH₃OH-CO₂ ice mixtures and their astrophysical implications. *Astron. Astrophys.* **1999**, *350*, 240–253.
- (11) Gerakines, P. A.; Whittet, D. C. B.; Ehrenfreund, P.; Boogert, A. C. A.; Tielens, A. G. G. M.; Schutte, W. A.; Chiar, J. E.; van Dishoeck, E. F.; Prusti, T.; Helmich, F. P.; de Graauw, T. Observations of Solid Carbon Dioxide in Molecular Clouds with the Infrared Space Observatory. *Astrophys. J.* **1999**, *522*, 357–377.
- (12) Boogert, A. C. A.; Ehrenfreund, P.; Gerakines, P. A.; Tielens, A. G. G. M.; Whittet, D. C. B.; Schutte, W. A.; van Dishoeck, E. F.; de Graauw, T.; Decin, L.; Prusti, T. ISO-SWS observations of interstellar solid ¹³CO₂: heated ice and the Galactic ¹²C/¹³C abundance ratio. *Astron. Astrophys.* **2000**, *353*, 349–362.
- (13) Pontoppidan, K. M.; Fraser, H. J.; Dartois, E.; Thi, W. F.; van Dishoeck, E. F.; Boogert, A. C. A.; d’Hendecourt, L.; Tielens, A. G. G. M.; Bisschop, S. E. A 3–5 μ m VLT spectroscopic survey of embedded young low mass stars I. Structure of the CO ice. *Astron. Astrophys.* **2003**, *408*, 981–1007.
- (14) Pontoppidan, K. M.; Boogert, A. C. A.; Fraser, H. J.; van Dishoeck, E. F.; Blake, G. A.; Lahuis, F.; Öberg, K. I.; Evans, I.; Neal, J.; Salyk, C. The c2d Spitzer Spectroscopic Survey of Ices around Low-Mass Young Stellar Objects. II. CO₂. *Astrophys. J.* **2008**, *678*, 1005–1031.

- (15) Brunken, N. G. C. et al. JWST observations of $^{13}\text{CO}_2$ ice. Tracing the chemical environment and thermal history of ices in protostellar envelopes. *Astron. Astrophys.* **2024**, *685*, A27.
- (16) Poteet, C. A.; Pontoppidan, K. M.; Megeath, S. T.; Watson, D. M.; Isokoski, K.; Bjorkman, J. E.; Sheehan, P. D.; Linnartz, H. Anomalous CO_2 Ice toward HOPS-68: A Tracer of Protostellar Feedback. *Astrophys. J.* **2013**, *766*, 117.
- (17) Isokoski, K.; Poteet, C. A.; Linnartz, H. Highly resolved infrared spectra of pure CO_2 ice (15–75 K). *Astron. Astrophys.* **2013**, *555*, A85.
- (18) Ehrenfreund, P.; Boogert, A. C. A.; Gerakines, P. A.; Jansen, D. J.; Schutte, W. A.; Tielens, A. G. G. M.; van Dishoeck, E. F. A laboratory database of solid CO and CO_2 for ISO. *Astron. Astrophys.* **1996**, *315*, L341–L344.
- (19) Dartois, E. Spectroscopic evidence of grain ice mantle growth in YSOs. I. CO ice modeling and limiting cases. *Astron. Astrophys.* **2006**, *445*, 959–970.
- (20) Dartois, E.; Noble, J. A.; Ysard, N.; Demyk, K.; Chabot, M. Influence of grain growth on CO_2 ice spectroscopic profiles. Modelling for dense cores and disks. *Astron. Astrophys.* **2022**, *666*, A153.
- (21) Brunken, N. G. C.; van Dishoeck, E. F.; Slavicinska, K.; le Gouellec, V. J. M.; Rocha, W. R. M.; Francis, L.; Tychoniec, L.; van Gelder, M. L.; Navarro, M. G.; Boogert, A. C. A.; Kavanagh, P. J.; Nazari, P.; Greene, T.; Ressler, M. E.; Majumdar, L. JOYS+ study of solid-state $^{12}\text{C}/^{13}\text{C}$ isotope ratios in protostellar envelopes: Observations of CO and CO_2 ice with the James Webb Space Telescope. *Astron. Astrophys.* **2024**, *692*, A163.
- (22) van Dishoeck, E. F. et al. The diverse chemistry of protoplanetary disks as revealed by JWST. *Faraday Discussions* **2023**, *245*, 52–79.

- (23) Beuther, H. et al. JWST Observations of Young protoStars (JOYS). Outflows and accretion in the high-mass star-forming region IRAS 23385+6053. *Astron. Astrophys.* **2023**, *673*, A121.
- (24) van Dishoeck, E. F. JWST Observations of Young protoStars (JOYS) Overview of program and early results. *Astron. Astrophys.* **2025**,
- (25) Federman, S. A. et al. Investigating Protostellar Accretion-driven Outflows across the Mass Spectrum: JWST NIRSpec Integral Field Unit 3–5 μm Spectral Mapping of Five Young Protostars. *Astrophys. J.* **2024**, *966*, 41.
- (26) Narang, M. et al. Discovery of a Collimated Jet from the Low-luminosity Protostar IRAS 16253-2429 in a Quiescent Accretion Phase with the JWST. *Astrophys. J. Lett.* **2024**, *962*, L16.
- (27) Rubinstein, A. E. et al. IPA: Class 0 Protostars Viewed in CO Emission Using JWST. *Astrophys. J.* **2024**, *974*, 112.
- (28) van Gelder, M. L. et al. JOYS+: Mid-infrared detection of gas-phase SO_2 emission in a low-mass protostar. The case of NGC 1333 IRAS 2A: Hot core or accretion shock? *Astron. Astrophys.* **2024**, *682*, A78.
- (29) Narang, M. et al. Discovery of a Collimated Jet from the Low-luminosity Protostar IRAS 16253-2429 in a Quiescent Accretion Phase with the JWST. *Astrophys. J. Lett.* **2024**, *962*, L16.
- (30) van Gelder, M. L. et al. JWST Observations of Young protoStars (JOYS): Overview of gaseous molecular emission and absorption in low-mass protostars. *Astron. Astrophys.* **2024**, *692*, A197.
- (31) Poteet, C. A.; Megeath, S. T.; Watson, D. M.; Calvet, N.; Remming, I. S.; McClure, M. K.; Sargent, B. A.; Fischer, W. J.; Furlan, E.; Allen, L. E.; Bjorkman, J. E.;

- Hartmann, L.; Muzerolle, J.; Tobin, J. J.; Ali, B. A Spitzer Infrared Spectrograph Detection of Crystalline Silicates in a Protostellar Envelope. *Astrophys. J. Lett.* **2011**, *733*, L32.
- (32) Kemper, F.; Vriend, W. J.; Tielens, A. G. G. M. The Absence of Crystalline Silicates in the Diffuse Interstellar Medium. *Astrophys. J.* **2004**, *609*, 826–837.
- (33) Slavicinska, K. et al. JWST detections of amorphous and crystalline HDO ice toward massive protostars. *Astron. Astrophys.* **2024**, *688*, A29.
- (34) van Broekhuizen, F. A.; Groot, I. M. N.; Fraser, H. J.; van Dishoeck, E. F.; Schlemmer, S. Infrared spectroscopy of solid CO-CO₂ mixtures and layers. *Astron. Astrophys.* **2006**, *451*, 723–731.
- (35) Rocha, W. R. M.; Rachid, M. G.; Olsthoorn, B.; van Dishoeck, E. F.; McClure, M. K.; Linnartz, H. LIDA: The Leiden Ice Database for Astrochemistry. *Astron. Astrophys.* **2022**, *668*, A63.
- (36) Dominik, C.; Min, M.; Tazaki, R. OpTool: Command-line driven tool for creating complex dust opacities. Astrophysics Source Code Library, record ascl:2104.010, 2021.
- (37) Tielens, A. G. G. M.; Tokunaga, A. T.; Geballe, T. R.; Baas, F. Interstellar Solid CO: Polar and Nonpolar Interstellar Ices. *Astrophys. J.* **1991**, *381*, 181.
- (38) Gerakines, P. A.; Schutte, W. A.; Greenberg, J. M.; van Dishoeck, E. F. The infrared band strengths of H₂O, CO and CO₂ in laboratory simulations of astrophysical ice mixtures. *Astron. Astrophys.* **1995**, *296*, 810.
- (39) Bouilloud, M.; Fray, N.; Bénilan, Y.; Cottin, H.; Gazeau, M. C.; Jolly, A. Bibliographic review and new measurements of the infrared band strengths of pure molecules at 25 K: H₂O, CO₂, CO, CH₄, NH₃, CH₃OH, HCOOH and H₂CO. *Mon. Not. R. Astron. Soc.* **2015**, *451*, 2145–2160.

- (40) Gerakines, P. A.; Bray, J. J.; Davis, A.; Richey, C. R. The Strengths of Near-Infrared Absorption Features Relevant to Interstellar and Planetary Ices. *Astrophys. J.* **2005**, *620*, 1140–1150.
- (41) Henning, T. Cosmic Silicates. *Annu. Rev. Astron. Astrophys.* **2010**, *48*, 21–46.
- (42) Oba, Y.; Watanabe, N.; Kouchi, A.; Hama, T.; Pirronello, V. Experimental Study of CO₂ Formation by Surface Reactions of Non-energetic OH Radicals with CO Molecules. *Astrophys. J. Lett.* **2010**, *712*, L174–L178.
- (43) Ioppolo, S.; van Boheemen, Y.; Cuppen, H. M.; van Dishoeck, E. F.; Linnartz, H. Surface formation of CO₂ ice at low temperatures. *Mon. Not. R. Astron. Soc.* **2011**, *413*, 2281–2287.
- (44) Pontoppidan, K. M. Spatial mapping of ices in the Ophiuchus-F core. A direct measurement of CO depletion and the formation of CO₂. *Astron. Astrophys.* **2006**, *453*, L47–L50.
- (45) Allamandola, L. J.; Sandford, S. A.; Tielens, A. G. G. M.; Herbst, T. M. Infrared Spectroscopy of Dense Clouds in the C-H Stretch Region: Methanol and “Diamonds”. *Astrophys. J.* **1992**, *399*, 134.
- (46) Dartois, E.; Demyk, K.; d’Hendecourt, L.; Ehrenfreund, P. Carbon dioxide-methanol intermolecular complexes in interstellar grain mantles. *Astron. Astrophys.* **1999**, *351*, 1066–1074.
- (47) An, D.; Ramírez, S. V.; Sellgren, K.; Arendt, R. G.; Adwin Boogert, A. C.; Robitaille, T. P.; Schultheis, M.; Cotera, A. S.; Smith, H. A.; Stolovy, S. R. Massive Young Stellar Objects in the Galactic Center. I. Spectroscopic Identification from Spitzer Infrared Spectrograph Observations. *Astrophys. J.* **2011**, *736*, 133.

- (48) Watson, W. D. Interstellar molecule reactions. *Reviews of Modern Physics* **1976**, *48*, 513–552.
- (49) Langer, W. D.; Graedel, T. E.; Frerking, M. A.; Armentrout, P. B. Carbon and oxygen isotope fractionation in dense interstellar clouds. *Astrophys. J.* **1984**, *277*, 581–604.
- (50) Langer, W. D.; Penzias, A. A. $^{12}\text{C}/^{13}\text{C}$ Isotope Ratio in the Local Interstellar Medium from Observations of $^{13}\text{C}^{18}\text{O}$ in Molecular Clouds. *Astrophys. J.* **1993**, *408*, 539.
- (51) He, J.; Emtiaz, S.; Boogert, A.; Vidali, G. The $^{12}\text{CO}_2$ and $^{13}\text{CO}_2$ Absorption Bands as Tracers of the Thermal History of Interstellar Icy Grain Mantles. *Astrophys. J.* **2018**, *869*, 41.
- (52) Dartois, E.; d’Hendecourt, L. Search for NH_3 ice in cold dust envelopes around YSOs. *Astron. Astrophys.* **2001**, *365*, 144–156.
- (53) Boogert, A. C. A.; Brewer, K.; Brittain, A.; Emerson, K. S. Survey of Ices toward Massive Young Stellar Objects. I. OCS, CO, OCN^- , and CH_3OH . *Astrophys. J.* **2022**, *941*, 32.

Supporting Information Available

Supporting information: Additional figures including continuum fittings in the $15\ \mu\text{m}$ region, alternative band profile fittings of the CO_2 ice bands with different laboratory spectra, band profile fitting of the $3.5\ \mu\text{m}$ methanol feature and tables containing properties of the two sources and the FWHM and central positions of the Gaussian curves fitted to the $^{13}\text{CO}_2$ ice band.

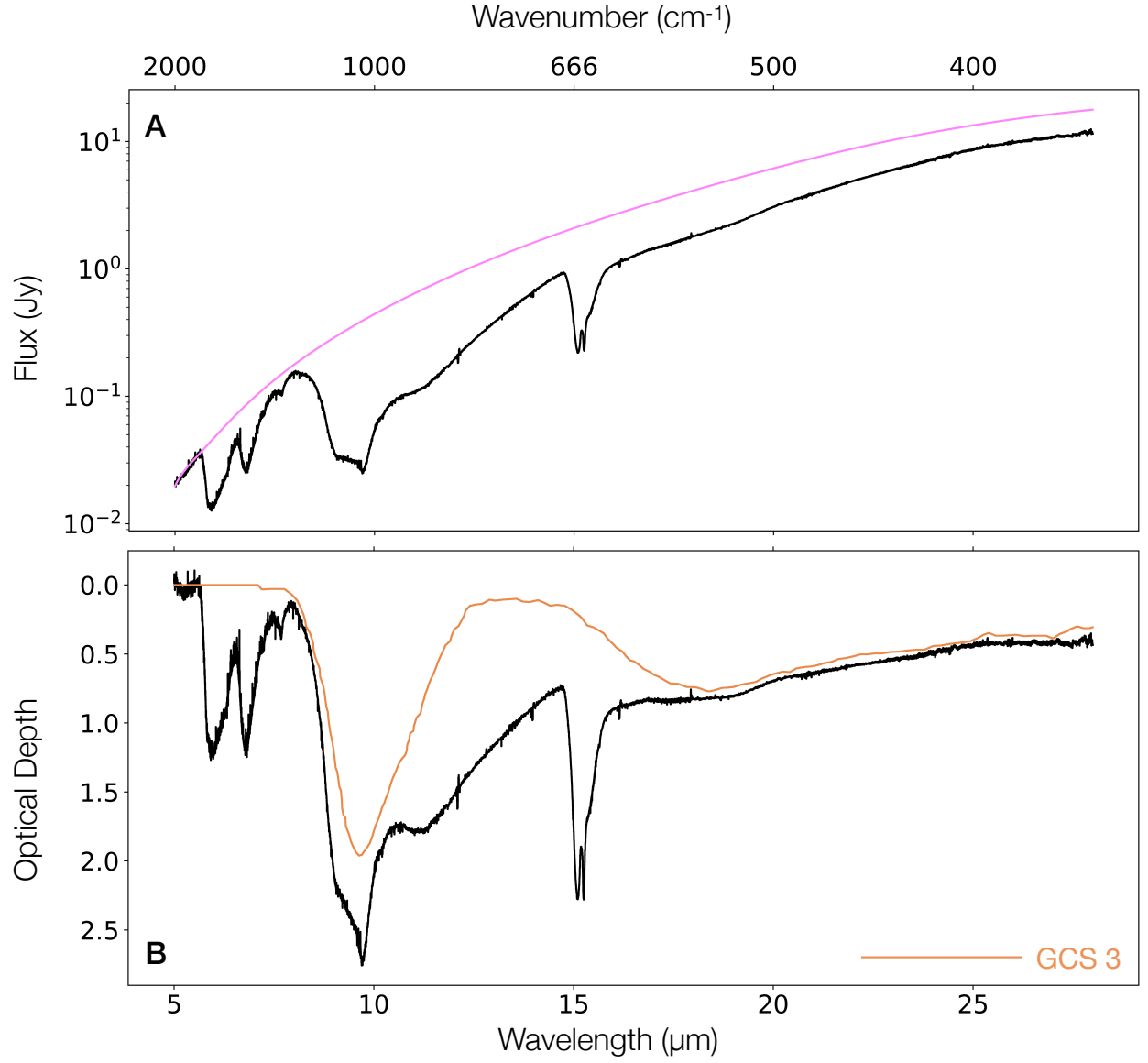


Figure 7: Continuum determination for Per-emb 35. Panel A shows the global continuum fitted over the 5 - 28 μm region (pink). Panel B shows the spectrum of GCS 3 fitted over the continuum subtracted spectrum (orange).

Table 6: Source properties.

Source	RA	Dec	L (L_{\odot})	Distance (pc)
IRAS 20126	20:14:26.04	41:13:32.43	10^4	1550
Per 35	3:28:37.093	31:13:30.83	9.3	293

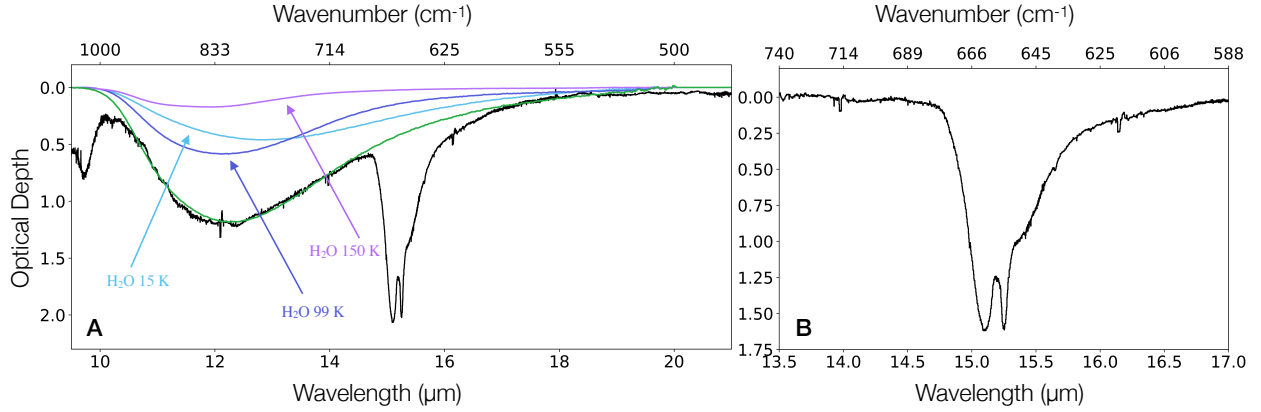


Figure 8: Subtraction of the water libration mode in Per-emb 35. Panel A shows the spectrum of water ice at different temperature fitted over the silicate subtracted spectrum. Panel B shows the final spectrum on optical depth scale.

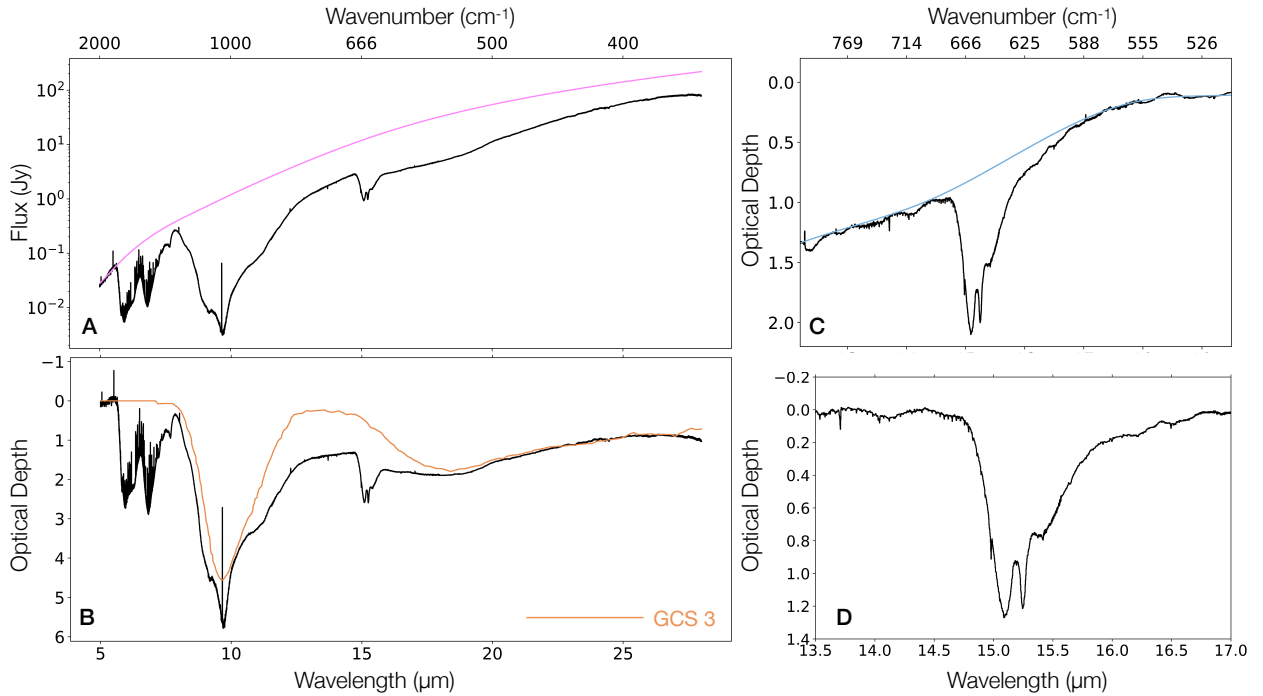


Figure 9: Continuum determination for IRAS 20126. Panel A shows the global continuum fitted over the 5 - 28 μm region (pink). Panel B shows the spectrum of GCS 3 fitted over the continuum subtracted spectrum (orange). Panel C shows the local continuum fitted over the silicate subtracted spectrum to simulate the wing of the water libration mode. Panel D shows the final spectrum on optical depth scale.

Table 7: Properties of the spectral features comprising the $^{13}\text{CO}_2$ band of IRAS 20126.

Component	Peak Position (cm^{-1})	FWHM (cm^{-1})
Long-wavelength	2275.72 ± 0.1	6.6 ± 0.1
Middle	2278.90 ± 0.4	9.0 ± 0.6
Short-wavelength	2282.91 ± 0.01	3.5 ± 0.1

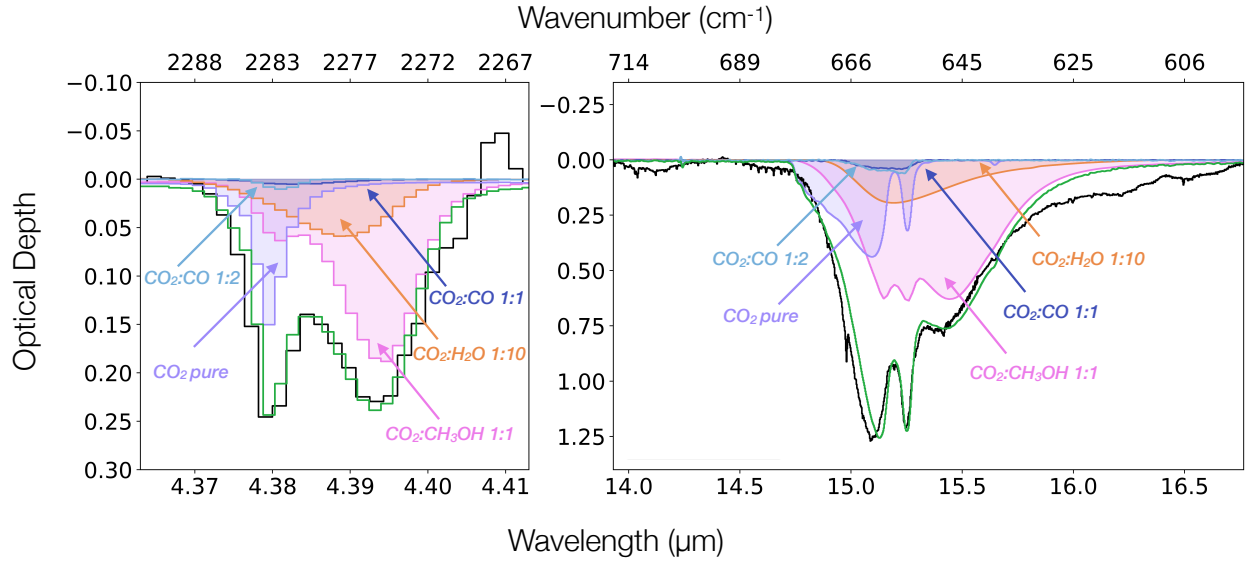


Figure 10: Alternative band profile analysis of IRAS 20126. Left: Decomposition of the $4.39 \mu\text{m}$ $^{13}\text{CO}_2$ band. Right: Decomposition of the $15.2 \mu\text{m}$ $^{12}\text{CO}_2$ band. The purple, pink, orange, light blue and dark blue shaded areas correspond to the pure CO_2 80 K, $\text{CO}_2:\text{CH}_3\text{OH}$ 1:1 115 K, $\text{CO}_2:\text{H}_2\text{O}$ 1:10 10 K, $\text{CO}_2:\text{CO}$ 1:2 25 K and $\text{CO}_2:\text{CO}$ 1:1 15 K component, respectively. Finally the green line shows the sum of all the components. The poor fit at $16.2 \mu\text{m}$ and $16.5 \mu\text{m}$ is likely due to absorption features of crystalline silicates.

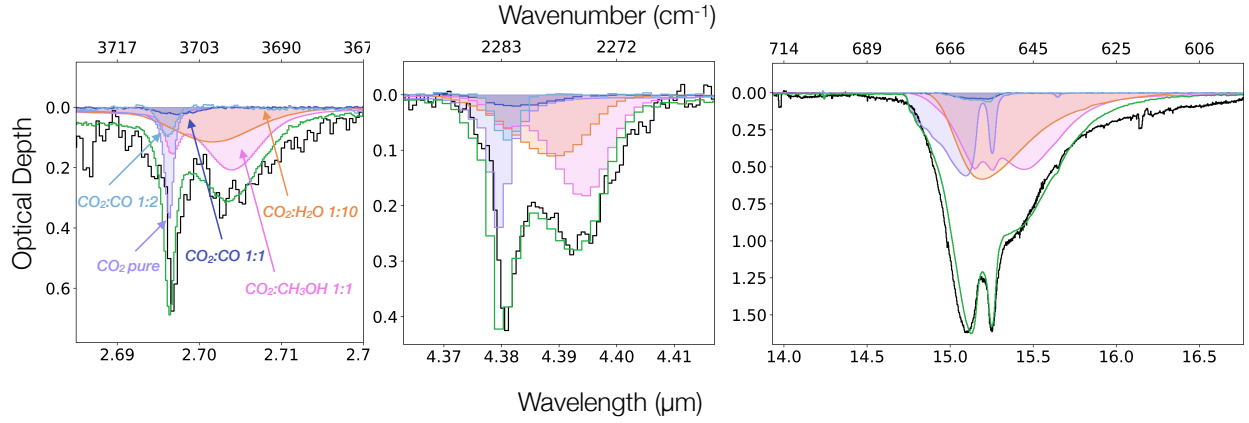


Figure 11: Alternative band profile analysis of Per-emb 35. Left: Decomposition of the $4.39 \mu\text{m}$ $^{13}\text{CO}_2$ band. Right: Decomposition of the $15.2 \mu\text{m}$ $^{12}\text{CO}_2$ band. The purple, pink, orange, light blue and dark blue shaded areas correspond to the pure CO_2 80 K, $\text{CO}_2:\text{CH}_3\text{OH}$ 1:1 115 K, $\text{CO}_2:\text{H}_2\text{O}$ 1:10 10 K, $\text{CO}_2:\text{CO}$ 1:2 25 K and $\text{CO}_2:\text{CO}$ 1:1 15 K component, respectively. Finally the green line shows the sum of all the components. The poor fit at $16.2 \mu\text{m}$ and $16.5 \mu\text{m}$ is likely due to absorption features of crystalline silicates.

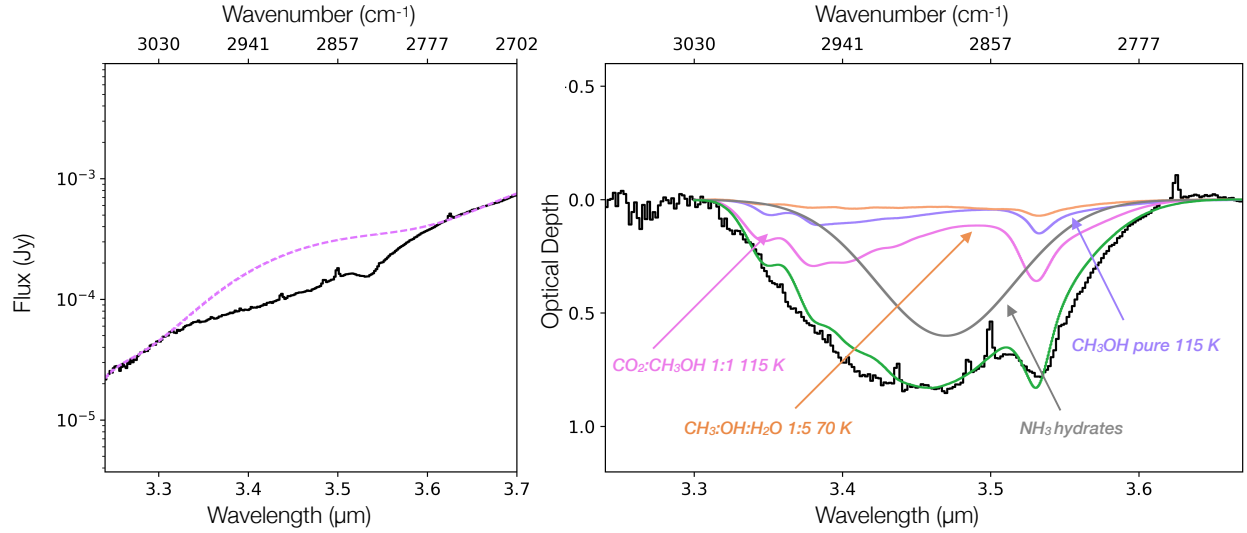


Figure 12: Continuum determination (left) and spectral decomposition (right) of the $3.5 \mu\text{m}$ CH_3OH feature. The purple, pink, orange, and gray lines correspond to spectra of pure CH_3OH 115 K, $\text{CO}_2:\text{CH}_3\text{OH}$ 1:1 115 K, $\text{H}_2\text{O}:\text{CH}_3\text{OH}$ 5:1 70 K and a Gaussian representing the ammonia hydrates in this region, respectively. The $\text{H}_2\text{O}:\text{CH}_3\text{OH}$ and pure CH_3OH spectra were obtained from Slavicinska et al.³³ and the properties of the Gaussian curve are based on the results presented in Boogert et al.⁵³.